Electronic Supplementary Information

Divalent transition metal ion intercalated hydrated V_2O_5 nanosheet cathodes for ultra-long cycling aqueous zinc-ion batteries

Jie Bai [a], Wenting Ji [b], Mengda Xue [a], De Li *[b], Huayu Wang [a], and Lingyun Chen*[a]

[a] Department of Applied Chemistry, School of Chemistry and Chemical Engineering, Chongqing University, Chongqing 401331, China

[b] State Key Laboratory of Marine Resources Utilization in South China Sea, Key Laboratory of Research on Utilization of Si-Zr-Ti Resources of Hainan Province, School of Materials Science and Engineering, Hainan University, Haikou 570228, China

*Corresponding authors.

* *E-mail addresses*: lidehainu@hainanu.edu.cn (D. Li), lychen@cqu.edu.cn (L. Chen)

Experimental section

Chemical Reagents

Vanadium pentoxide (V_2O_5, AR), *N*-methyl-2-pyrrolidone (NMP, AR), and polyvinylidene fluoride (PVDF) were purchased from Chengdu Kelong Chemical Co., Ltd. The deionized water used in this study was derived from Wahaha purified water, produced by Hangzhou Wahaha Group Co., Ltd. Hydrogen peroxide (H_2O_2, AR, 30 wt% in H_2O) was supplied by Chuandong Chemical (Group) Co. Ltd. (Chongqing, China). Cobalt chloride hexahydrate ($CoCl_2 \cdot 6H_2O$, 99%), Nickel chloride hexahydrate ($NiCl_2 \cdot 6H_2O$, 99%), and Cupric Chloride Anhydrous ($CuCl_2$, 98%) was purchased from the Adamas brand, offered by Shanghai Titan Scientific Co., Ltd. Acetylene black was purchased from Cyber Electrochemical Materials Network. Zinc trifluoromethanesulfonate ($Zn(CF_3SO_3)_2$, 98 %) was purchased from Shanghai Dibo Biotechnology Co., Ltd. All chemical reagents were utilized without any further processing and purification.

Preparation of pristine $V_2O_5 \cdot nH_2O$

We introduced modifications to previously reported synthetic methods.[1] Initially, commercial V_2O_5 powder (363.8 mg, 2.00 mmol) was dispersed in 27 mL of deionized water. Subsequently, 8 mL of H_2O_2 solution (30 wt%) was added to the dispersion and stirred at room temperature for 120 minutes, yielding a clear wine-red solution. This solution was then transferred into a 100 mL Teflon-lined stainless-steel autoclave and subjected to hydrothermal treatment at 200°C for 3 hours, resulting in the formation of an orange hydrosol composed of $V_2O_5 \cdot nH_2O$ nanosheets. Finally, the obtained orange hydrosol was freeze-dried at −50°C for 48 hours to yield the final product.

Preparation of Co-$V_2O_5 \cdot nH_2O$, Ni-$V_2O_5 \cdot nH_2O$, and Cu-$V_2O_5 \cdot nH_2O$ nanosheets

Building upon the preparation of the $V_2O_5 \cdot nH_2O$ nanosheet hydrosol, the next steps involved the intercalation of transition metal cations. First, the orange $V_2O_5 \cdot nH_2O$ nanosheet hydrosol was diluted with 150 mL of deionized water. Then, a certain amount of 0.2 mol L^{-1} $CoCl_2$ solution was added dropwise under continuous stirring to facilitate the colloidal self-assembly process. After stirring for 5 hours, the self-assembled flocculated product was collected, washed several times with deionized water, and filtered. The filtered product was subsequently dried in a vacuum oven at 80°C for 24 hours to obtain the Co^{2+}-intercalated self-assembled sample. Similarly, the synthesis of Ni^{2+}- and Cu^{2+}-intercalated self-assembled samples followed the same procedure, with the 0.2 mol L^{-1} $CoCl_2$ solution replaced by equimolar $NiCl_2$ or $CuCl_2$ solutions, respectively.

Materials characterization

The X-ray diffraction (XRD) analysis was conducted using a Bruker D8 Advance powder diffractometer with Cu Kα radiation ($\lambda = 1.5406$ Å) to determine the crystal structure information. Fourier transform infrared (FTIR) spectroscopy was performed using a Bruker Tensor 27 spectrometer. Raman spectra were tested using laser confocal Raman spectrometer (LabRAM HR Evolution) under 532 nm laser excitation. X-ray photoelectron spectroscopy (XPS) tests were conducted on the Shimadzu/Krayos AXIS Ultra DLD. Inductively coupled plasma optical emission spectrometer (ICP-OES, Agilent 5800) was used to analyze the element compositions and ratios. Thermogravimetric analysis (TGA, Mettler Toledo TGA2) was conducted to detect the content of structural water. The morphology and microstructure were observed through field emission scanning electron microscope (FESEM) and environmental scanning electron microscope (ESEM, Quattro S), and field emission transmission electron microscope (FETEM, Talos F200S) with energy dispersive spectrometer (EDS). Characterization of the sample's surface structure was conducted using atomic force microscopy (AFM, MFP-3D-BIO). The volumetric changes of the electrode during the charge-discharge cycling were observed using in situ optical microscopy (OM, ZEISS Smartzoom5).

Electrochemical measurements

Carbon paper was used as the current collector, and a slurry was prepared by thoroughly mixing and grinding PVDF, acetylene black, and the active material in a mass ratio of 1:2:7 using NMP as the solvent. The resulting slurry was then evenly coated onto the carbon paper and vacuum dried at 80°C for 12 hours. The mass of the active material coated on the carbon paper was precisely controlled to be within the range of 0.9~1.2 mg cm^{-2}. The aqueous ZIBs were assembled with zinc metal anode, glass fiber separator (Whatman, GF/D), 2 M $Zn(CF_3SO_3)_2$ electrolyte, and carbon paper cathode. Galvanostatic charge/discharge (GCD) measurements was conducted via the LAND battery testing system (CT3001A). Cyclic voltammetry (CV) and electrochemical impedance spectroscopy (EIS, frequency range: 0.01 Hz to 100 kHz) were performed with the Bio-Logic SAS electrochemical workstation (VSP-300). Galvanostatic intermittent titration technique (GITT) was performed with the HOKUTO DENKO (HJ1001SD8) electrochemical testing system.

Computational methods

All density functional theory (DFT) calculations were carried out using the Vienna Ab initio Simulation Package (VASP),[2] with DFT + U corrections applied to the V and Co atoms.[3] The Kohn-Sham equations were solved using the projector augmented-wave (PAW) approach,[4, 5] and the exchange-correlation functional was taken using the generalized gradient approximation (GGA) as constructed by Perdew-Burke-Ernzerhof (PBE).[6, 7] In this work, the Γ-centered k-grid scheme

(2×3×2) was employed, and all investigated structures were fully relaxed with a cutoff energy of 480 eV. During this process, the force convergence criterion was set to 10^{-2} eV Å^{-1}, and the energy convergence criterion was set to 10^{-5} eV. A monolayer V_2O_5 structure was constructed based on the optimized bulk V_2O_5.

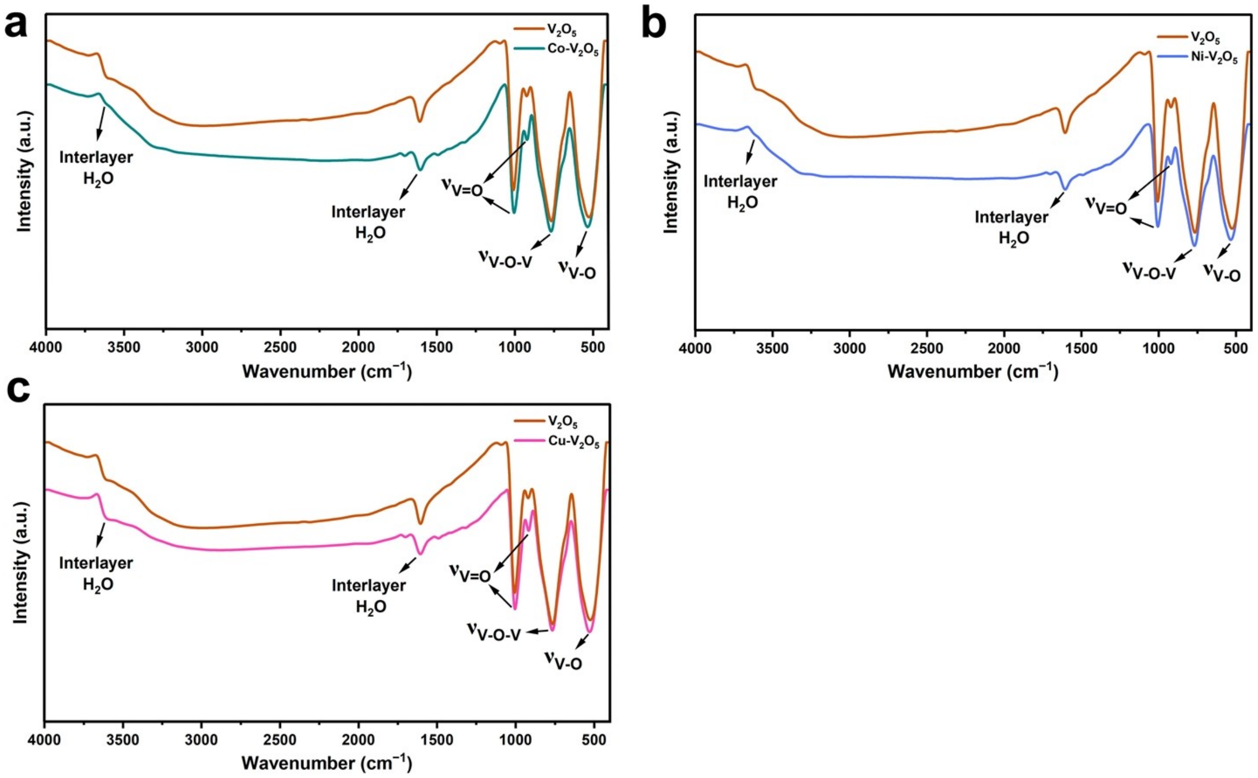

Fig. S1 FITR spectra of the $Co_{0.14}V_2O_5\cdot0.95H_2O$, $Ni_{0.15}V_2O_5\cdot0.63H_2O$, and $Cu_{0.15}V_2O_5\cdot0.60H_2O$. The characteristic peaks located at around 3609 cm^{-1} and 1605 cm^{-1} confirm the existence of interlayer crystal water in the flocculation product. It is noteworthy that, compared to freeze-dried bare V_2O_5, the bending vibration peaks of the Co^{2+}, Ni^{2+}, and Cu^{2+}intercalated samples are slightly weakened, indicating that they are confined to a low hydration state, resulting in relatively smaller d-spacing.[1]

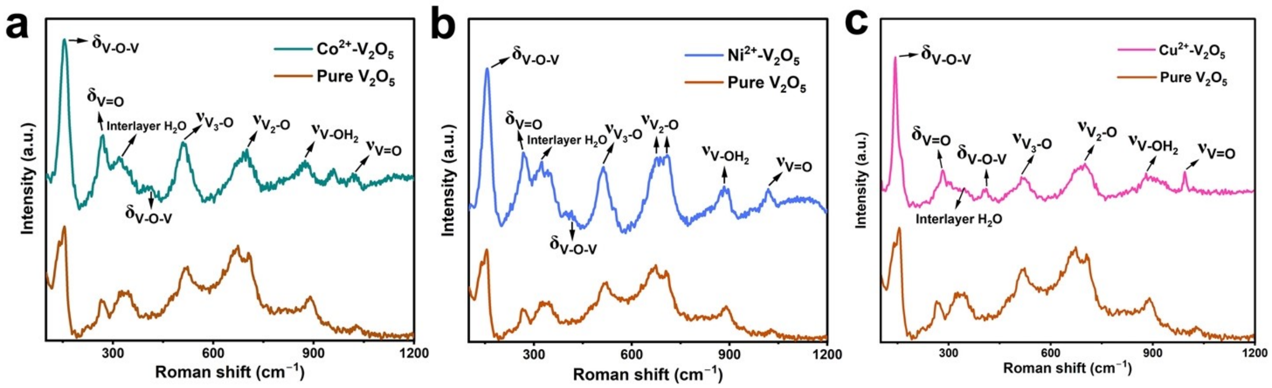

Fig. S2 Raman spectra of the $Co_{0.14}V_2O_5\cdot0.95H_2O$, $Ni_{0.15}V_2O_5\cdot0.63H_2O$, and $Cu_{0.15}V_2O_5\cdot0.60H_2O$ by the hydrosol ion-mediated self-assembly. The characteristic peaks at around 270 cm^{-1} and 1017 cm^{-1} are assigned to the bending vibration and terminal oxygen (V=O) stretching mode, respectively. The characteristic peaks of the bending vibration of V-O-V chains can be detected at 157 cm^{-1} and 416 cm^{-1}. The characteristic peak at 704 cm^{-1} are assigned to disordered stretching vibration of V_2-O (doubly coordinated oxygen) bonds, and the peak at 513 cm^{-1} originates from the stretching vibration of V_3-O (triply coordinated oxygen) bonds.

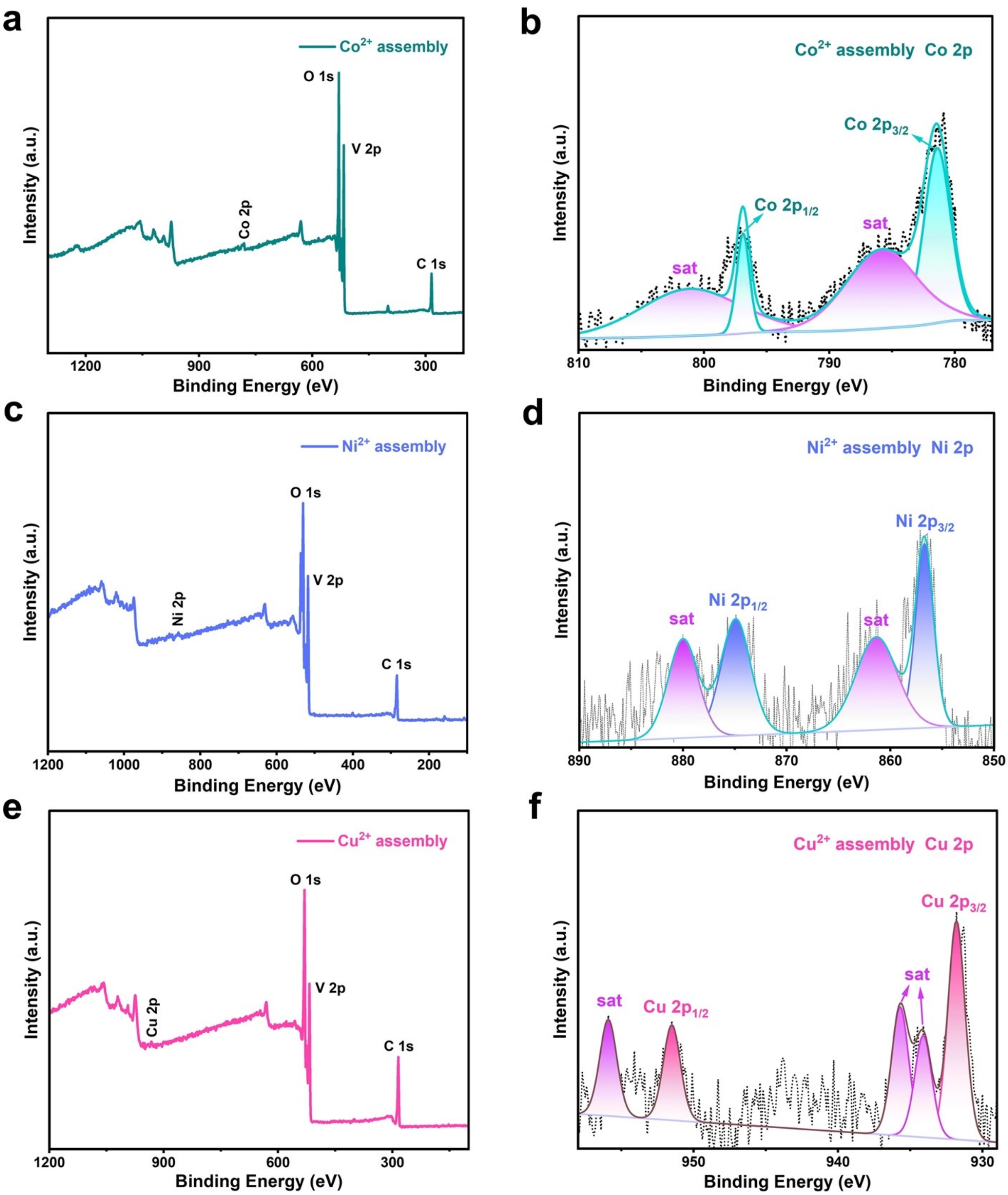

Fig. S3 XPS spectra of the $Co_{0.14}V_2O_5 \cdot 0.95H_2O$, $Ni_{0.15}V_2O_5 \cdot 0.63H_2O$, and $Cu_{0.15}V_2O_5 \cdot 0.60H_2O$.

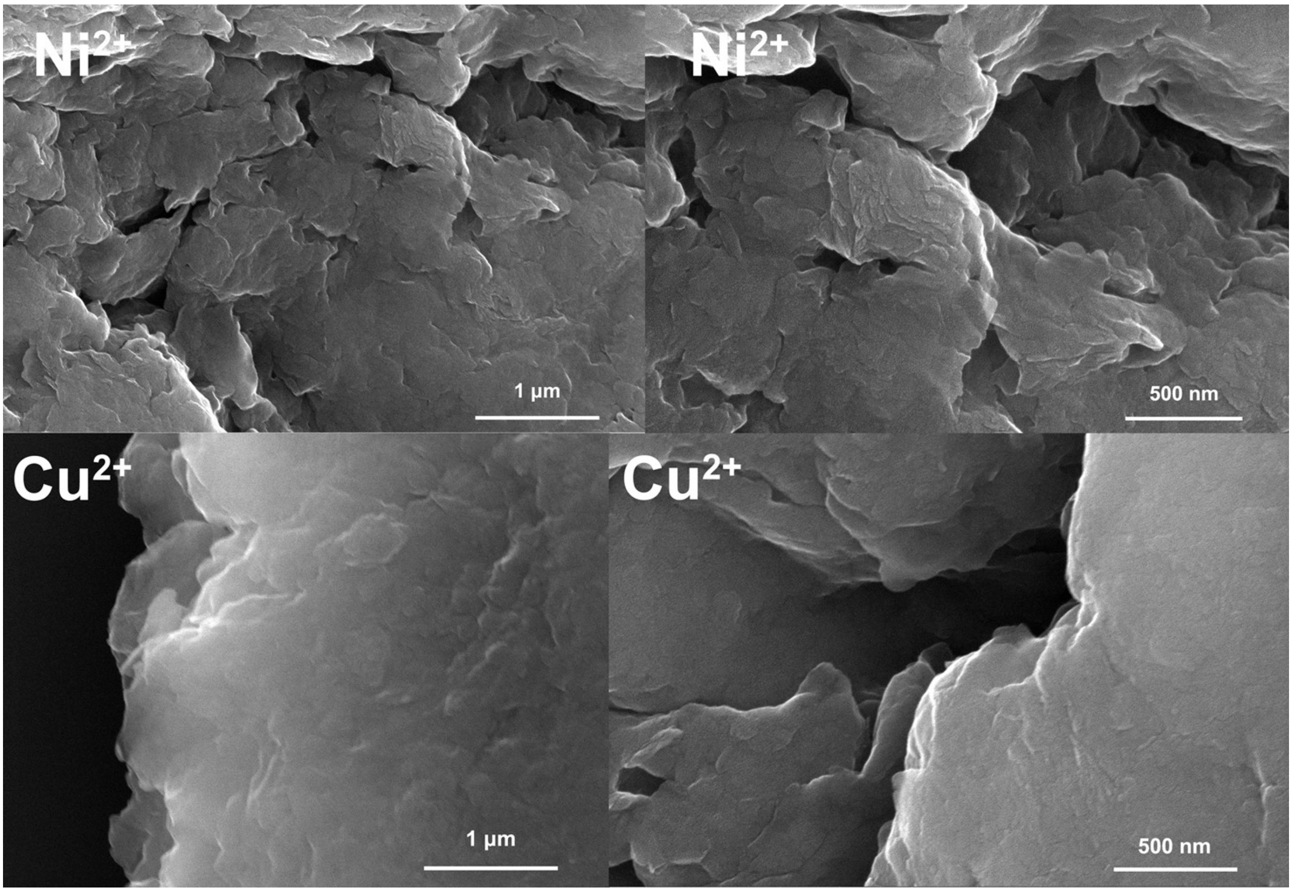

Fig. S4 ESEM images of $Ni_{0.15}V_2O_5 \cdot 0.63H_2O$, and $Cu_{0.15}V_2O_5 \cdot 0.60H_2O$.

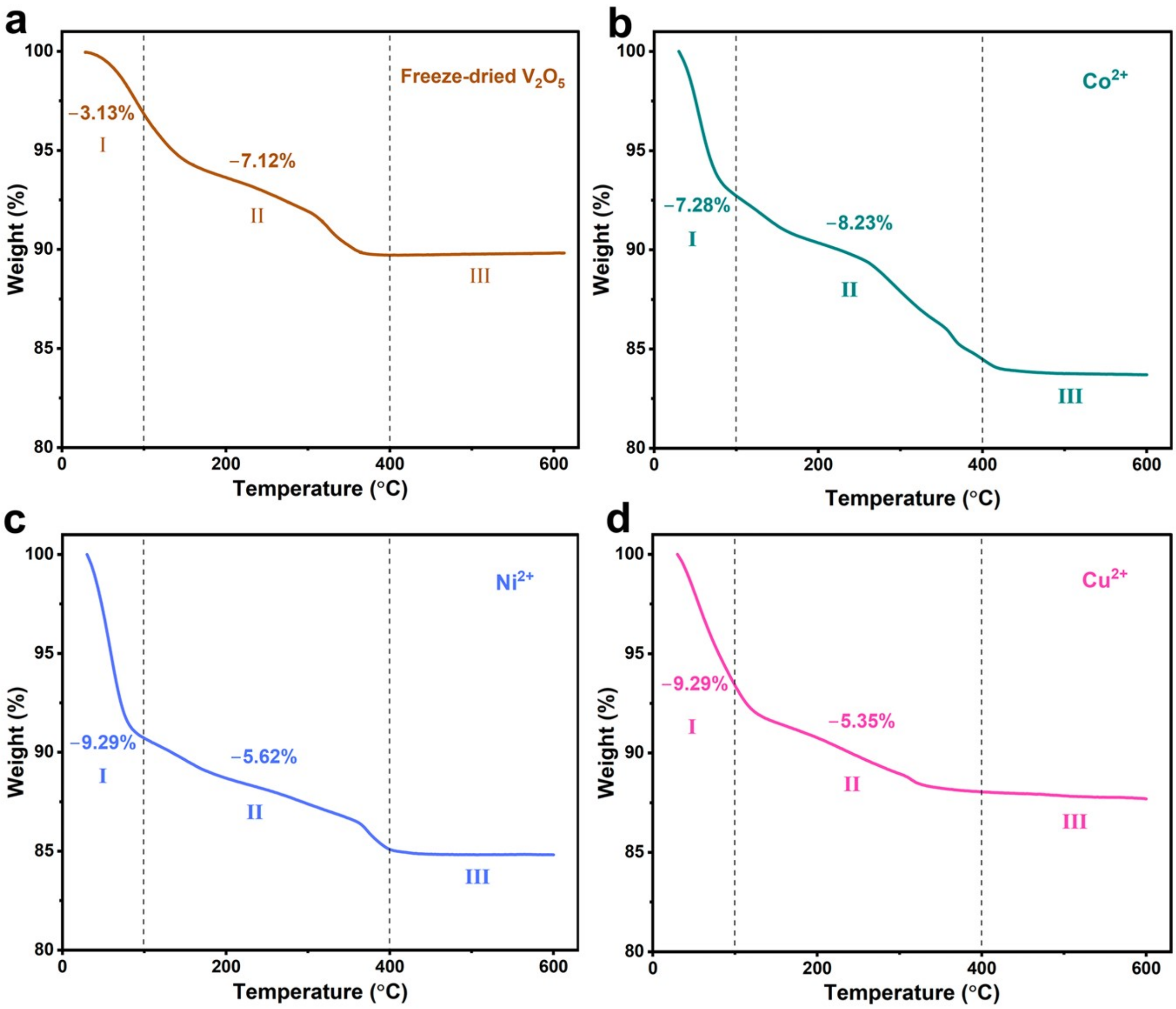

Fig. S5 The TGA was conducted for pristine $V_2O_5 \cdot nH_2O$ and the intercalated samples with Co^{2+}, Ni^{2+}, and Cu^{2+}, respectively, within the temperature range of 25–600 °C. The TGA analysis results of (a) $V_2O_5 \cdot 0.77H_2O$, (b) $Co_{0.14}V_2O_5 \cdot 0.95H_2O$, (c) $Ni_{0.15}V_2O_5 \cdot 0.63H_2O$, and (d) $Cu_{0.15}V_2O_5 \cdot 0.60H_2O$. The weight loss below 100°C (Region I) is attributed to the removal of adsorbed water, while the weight loss between 100°C and 400°C (Region II) corresponds to the evaporation of crystalline water.

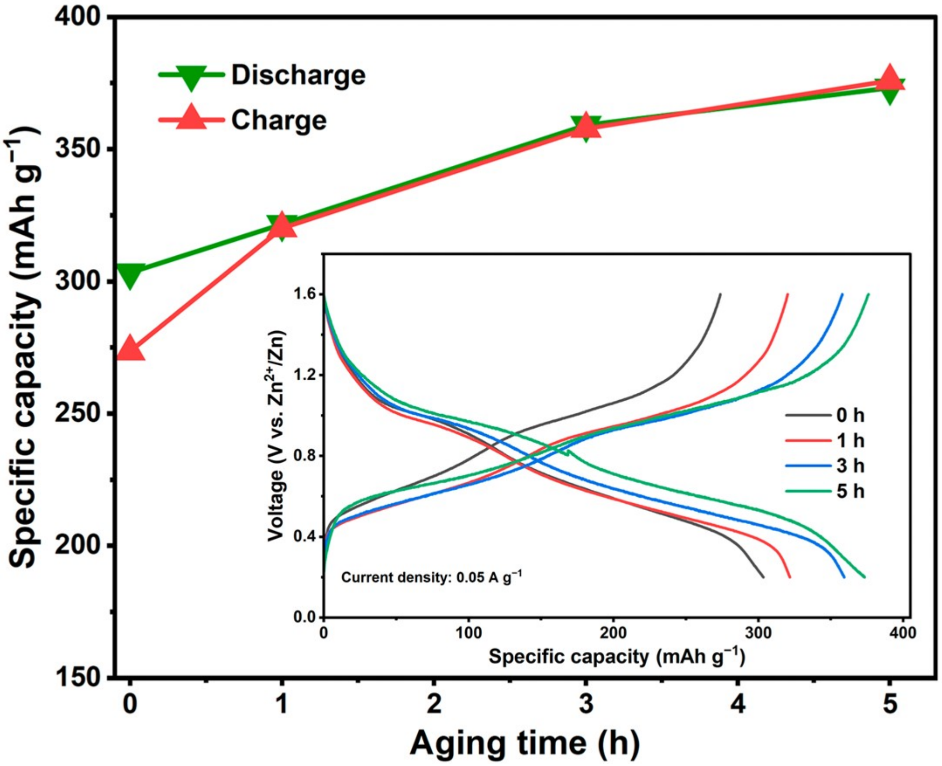

Fig. S6 The Relationship diagram of specific capacity with the aging time of the $Co_{0.14}V_2O_5 \cdot 0.95H_2O$ cathode at a current density of 0.05 A g^{-1}.

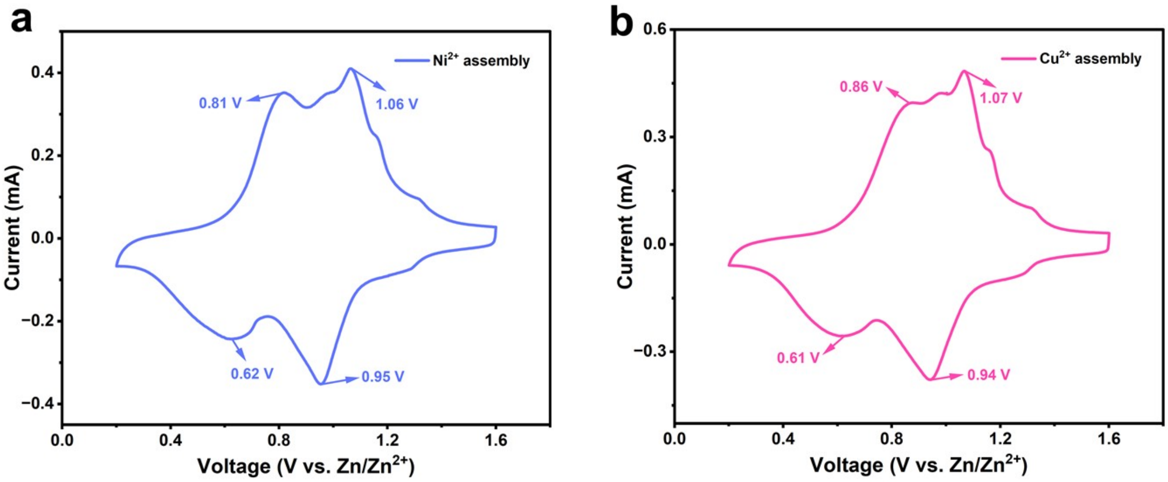

Fig. S7 CV profiles of (a) $Ni_{0.15}V_2O_5\cdot0.63H_2O$ and (b) $Cu_{0.15}V_2O_5\cdot0.60H_2O$ cathodes at a current density of 5.0 A g^{-1}.

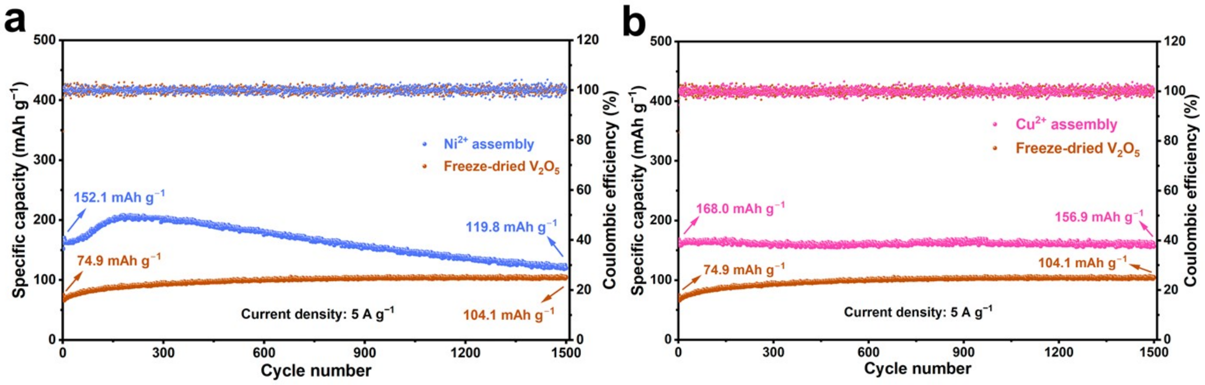

Fig. S8 Long-term cycling performance of (a) $Ni_{0.15}V_2O_5·0.63H_2O$ and (b) $Cu_{0.15}V_2O_5·0.60H_2O$ cathodes at a current density of 5.0 A g^{-1}.

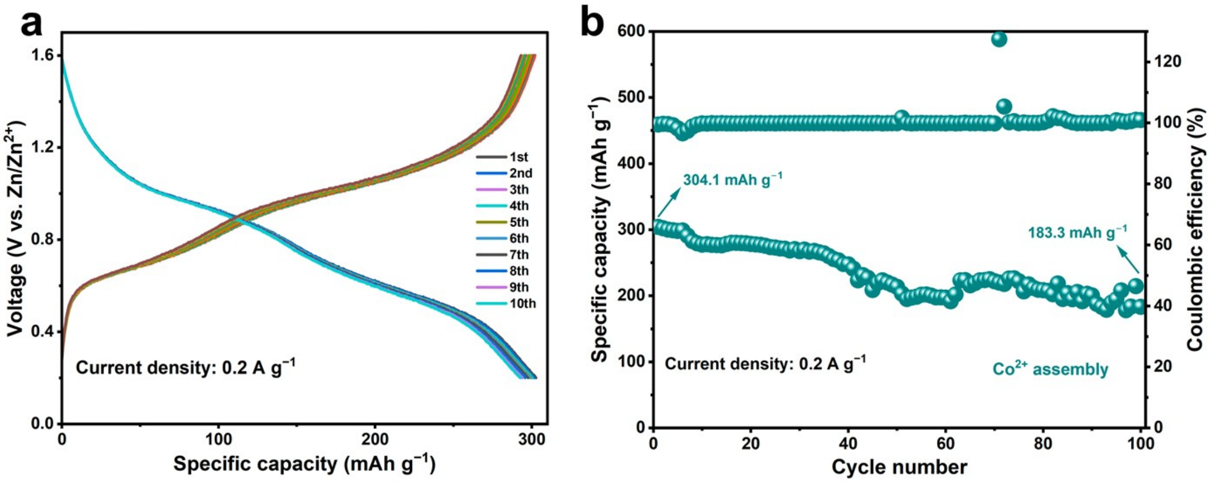

Fig. S9 The GCD curves and low-current cycling performance profiles of the $Co_{0.14}V_2O_5\cdot 0.95H_2O$ cathode.

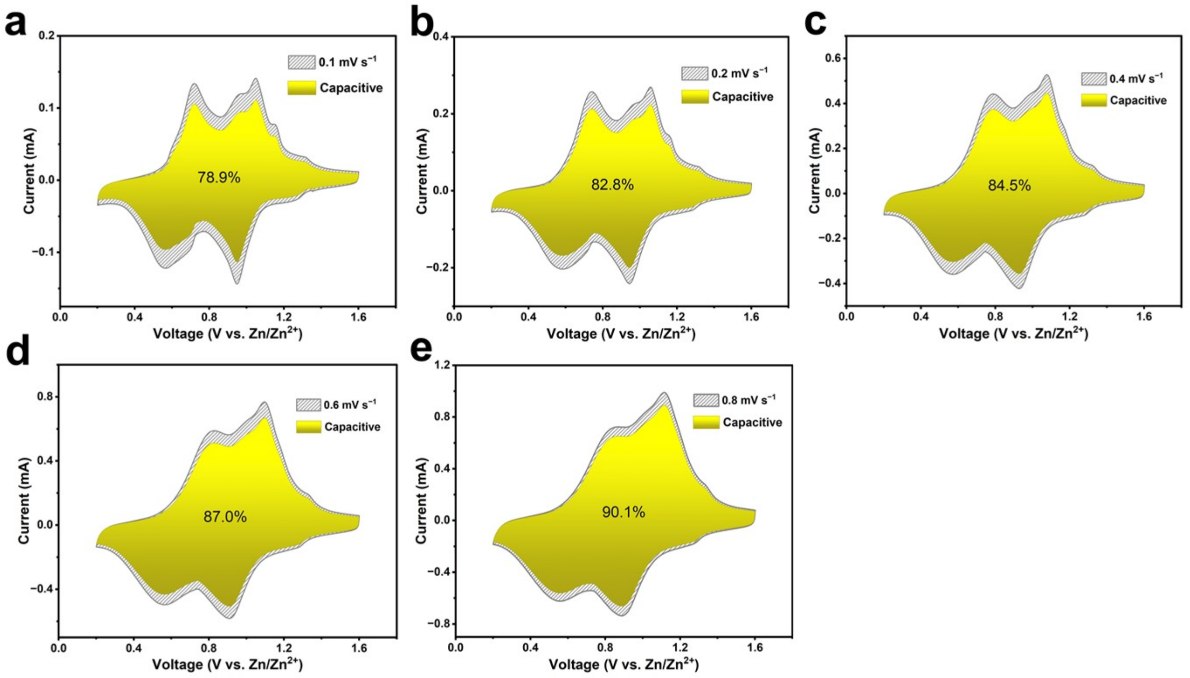

Fig. S10 The capacitive contribution diagrams of $Co_{0.14}V_2O_5 \cdot 0.95H_2O$ cathode at different scanning rate.

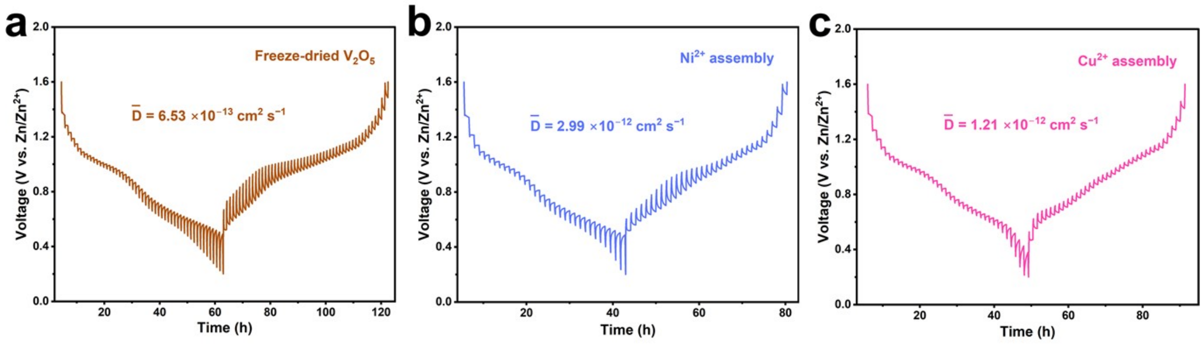

Fig. S11 The GITT diagrams of $V_2O_5 \cdot 0.77H_2O$, $Ni_{0.15}V_2O_5 \cdot 0.63H_2O$, and $Cu_{0.15}V_2O_5 \cdot 0.60H_2O$ cathodes.

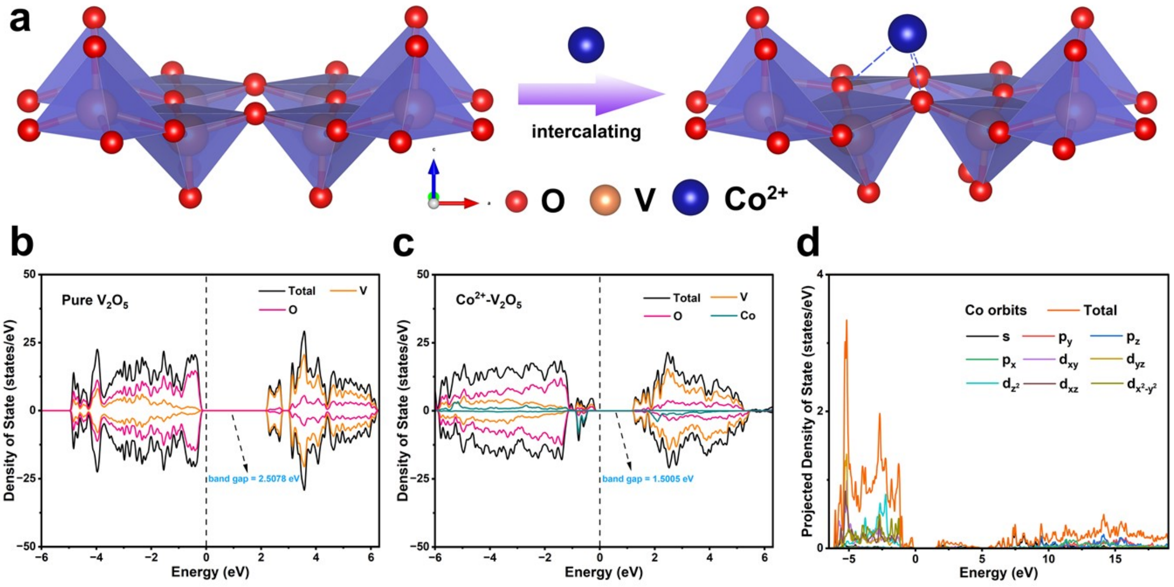

Fig. S12 (a) Schematic representations of the optimized structures of pristine V_2O_5 and Co^{2+}-intercalated V_2O_5. (b) and (c) TDOS and band structure calculations, including band gap values, for pristine V_2O_5 and Co^{2+}-intercalated V_2O_5. (d) PDOS for Co orbits in Co^{2+}-intercalated V_2O_5.

We employed DFT calculations to investigate the influence of Co^{2+} intercalation on the electronic structure of layered V_2O_5. We constructed monolayer models of pristine and Co^{2+}-intercalated V_2O_5, optimized their geometrical structures, and computed their respective density of states (DOS) and band structures. As shown in **Fig. S12a**, the insertion of Co slightly distorts the original V-O bonds, affecting the chemical coordination environment of pristine V_2O_5, which may impact the crystallinity of V_2O_5 post-intercalation. These findings are consistent with the observed weakening of the (001) peak in XRD patterns post Co^{2+} intercalation. The DOS calculations reveal that, compared to pristine V_2O_5, Co^{2+} intercalation increases the total density of states (TDOS) near the Fermi level (**Fig. S12b** and **c**). Moreover, Co^{2+} intercalation shifts the conduction band (CB) closer to the Fermi level, resulting in a reduced band gap. To verify these results, we calculated the band structures of both pristine and Co^{2+}-intercalated V_2O_5. The calculations indicate a significant reduction in band gap post Co^{2+} intercalation (**Fig. S12b** and **c**), corroborating the DOS results. To further explore the impact of Co insertion on the electronic structure of V_2O_5, we also computed the projected density of states (PDOS) for Co. The results show a substantial contribution of Co's electronic states near the Fermi level, primarily from the d_{z^2}, d_{xz}, and $d_{x^2-y^2}$ orbitals (**Fig. S12d**). The PDOS results of Co align well with the observed shift of the CB toward the Fermi level upon Co^{2+}-intercalated V_2O_5.

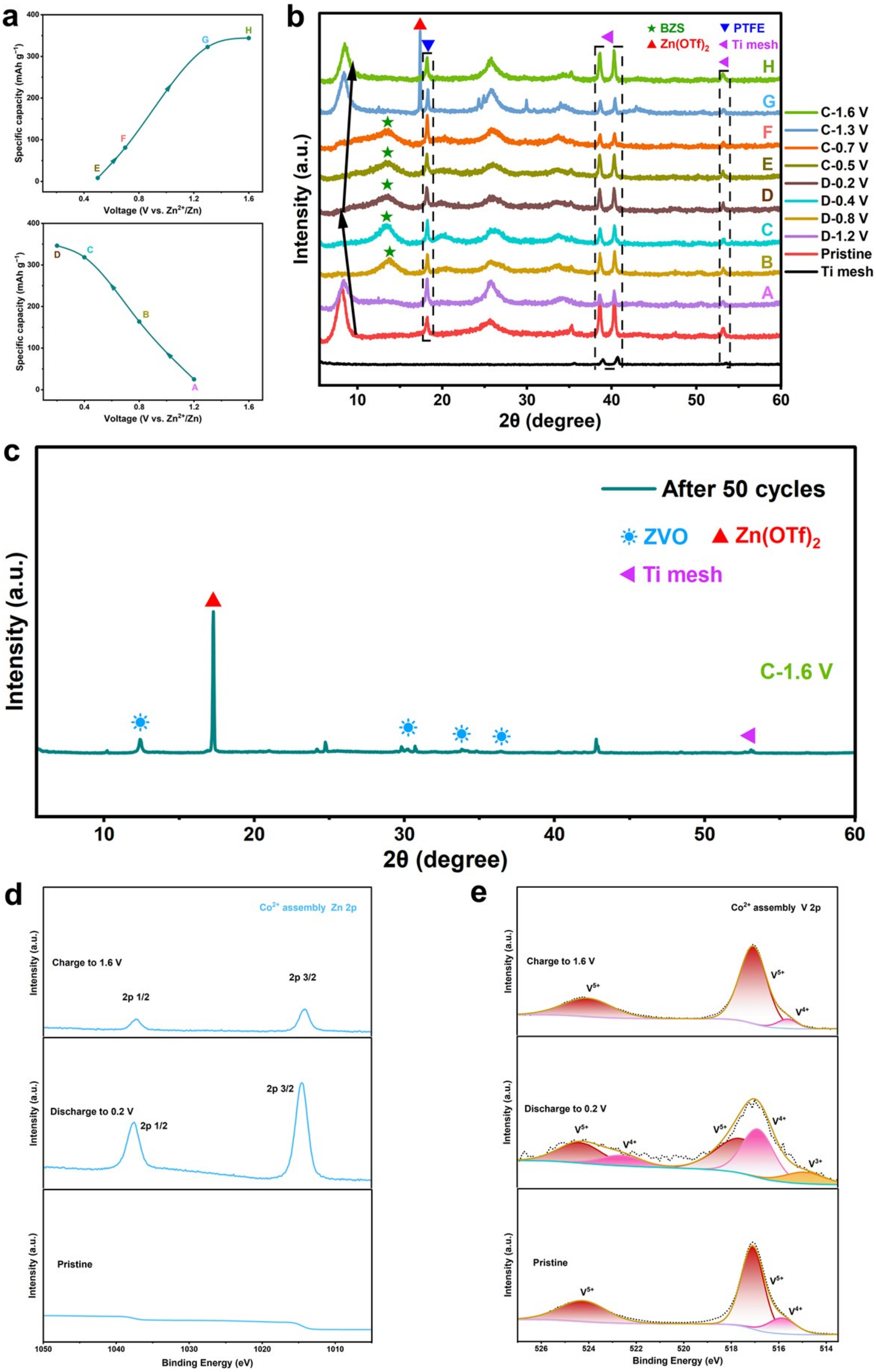

Fig. S13 (a) and (b) The discharge-charge curves of different states and ex situ XRD pattern of $Co_{0.14}V_2O_5\cdot 0.95H_2O$ cathode. (c) Ex situ XRD pattern of $Co_{0.14}V_2O_5\cdot 0.95H_2O$ cathode charged to 1.6 V after 50 cycles. (d) and (e) The Zn and V 2p region of the XPS spectra with pristine, discharge to 0.2 V and charge to 1.6 V states of $Co_{0.14}V_2O_5\cdot 0.95H_2O$.

We conducted ex situ XRD analysis at various potentials during the first charge-discharge cycle at a current density of 0.1 A g^{-1} (**Fig. S13a** and **b**). At the onset of discharge, a very slight lattice contraction was observed, implying that the intercalated Zn ions screen the interlayer electrostatic repulsion.[8] During the first discharge cycle, a basic zinc salt (BZS) phase containing the OTf^{-} anion, corresponding to $Zn_{12}(CF_3SO_3)_9(OH)_{15}\cdot nH_2O$, was detected near 2θ ~13.4.[9-11] However, with increasing cycle numbers, the intensity of the BZS peak diminishes, ultimately leading to the formation of a more stable the zinc pyrovanadate phase (ZVO, $Zn_3V_2O_7(OH)_2\cdot nH_2O$).[10] After 50 cycles at a current density of 0.2 A g^{-1}, ex situ XRD analysis of $Co_{0.14}V_2O_5\cdot 0.95H_2O$ cathode clearly detected the presence of the ZVO phase, while the BZS phase had disappeared. These results provide strong evidence supporting the aforementioned conclusion (**Fig. S13c**). Notably, ex-situ XRD results at any selected state within the first cycle do not exhibit any peaks associated with the ZVO phase, indicating that the ZVO phase does not form during the initial stage of electrochemical charge/discharge process.[10] Moreover, as the charging process progresses, the restoration of peaks corresponding to the initial phase prior to discharge was observed, indicating excellent reversibility of the $Co_{0.14}V_2O_5\cdot 0.95H_2O$ cathode during the electrochemical cycling process. Previous studies have indicated that the formation of the ZVO within the aqueous solution containing Zn ions is related to the dissolution of vanadium pentoxide, and the subsequent precipitation via the following reactions.[10, 12-14]

Dissolution: $V_2O_5 + 3H_2O \rightarrow 2VO_2(OH)_2^{-} + 2H^{+}$ (1)

Precipitation: $2VO_2(OH)_2^{-} + 3Zn^{2+} + 3H_2O \rightarrow Zn_3V_2O_7(OH)_2\cdot 2H_2O$ (ZVO) $+ 4H^{+}$ (2)

According to the aforementioned equations, the cathodic reaction processes necessitate the consumption of OH^{-} ions and the release of H^{+} ions, which will result in an increase in H^{+} concentration. Therefore, to maintain charge neutrality, H^{+} ions will intercalate into the interlayer of $Co_{0.14}V_2O_5\cdot 0.95H_2O$, ensuring stable cycling within the AZIBs system.[12, 15] The aforementioned results indicate that during the discharge process, Zn^{2+} and H^{+} are co-intercalated into the $Co_{0.14}V_2O_5\cdot 0.95H_2O$ layers. XPS spectra identify the reversible $V^{5+} \leftrightarrow V^{4+}/V^{3+}$ transition accompanying Zn^{2+} insertion and extraction processes (**Fig. S13d** and **e**), and these results at different charge-discharge states similarly reveal the intercalation/deintercalation mechanism of Zn^{2+} in the $Zn/Co_{0.14}V_2O_5 \cdot 0.95H_2O$ battery.

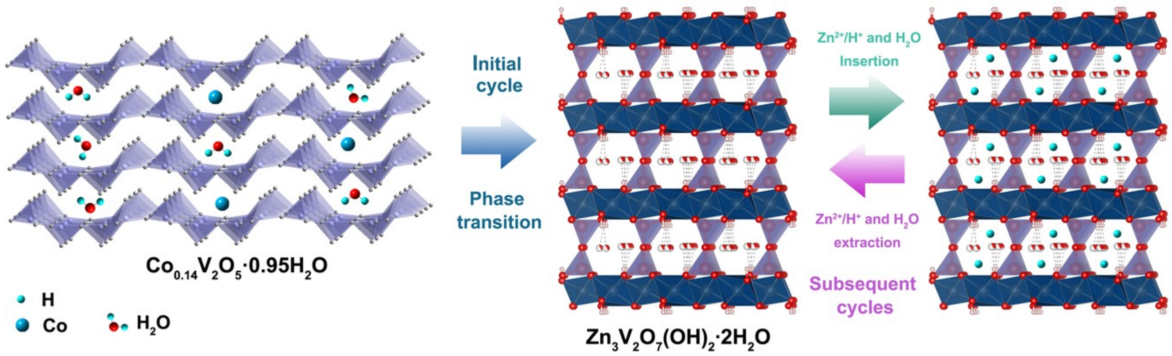

Fig. S14 The electrochemical reaction mechanism of $Co_{0.14}V_2O_5·0.95H_2O$ cathode.

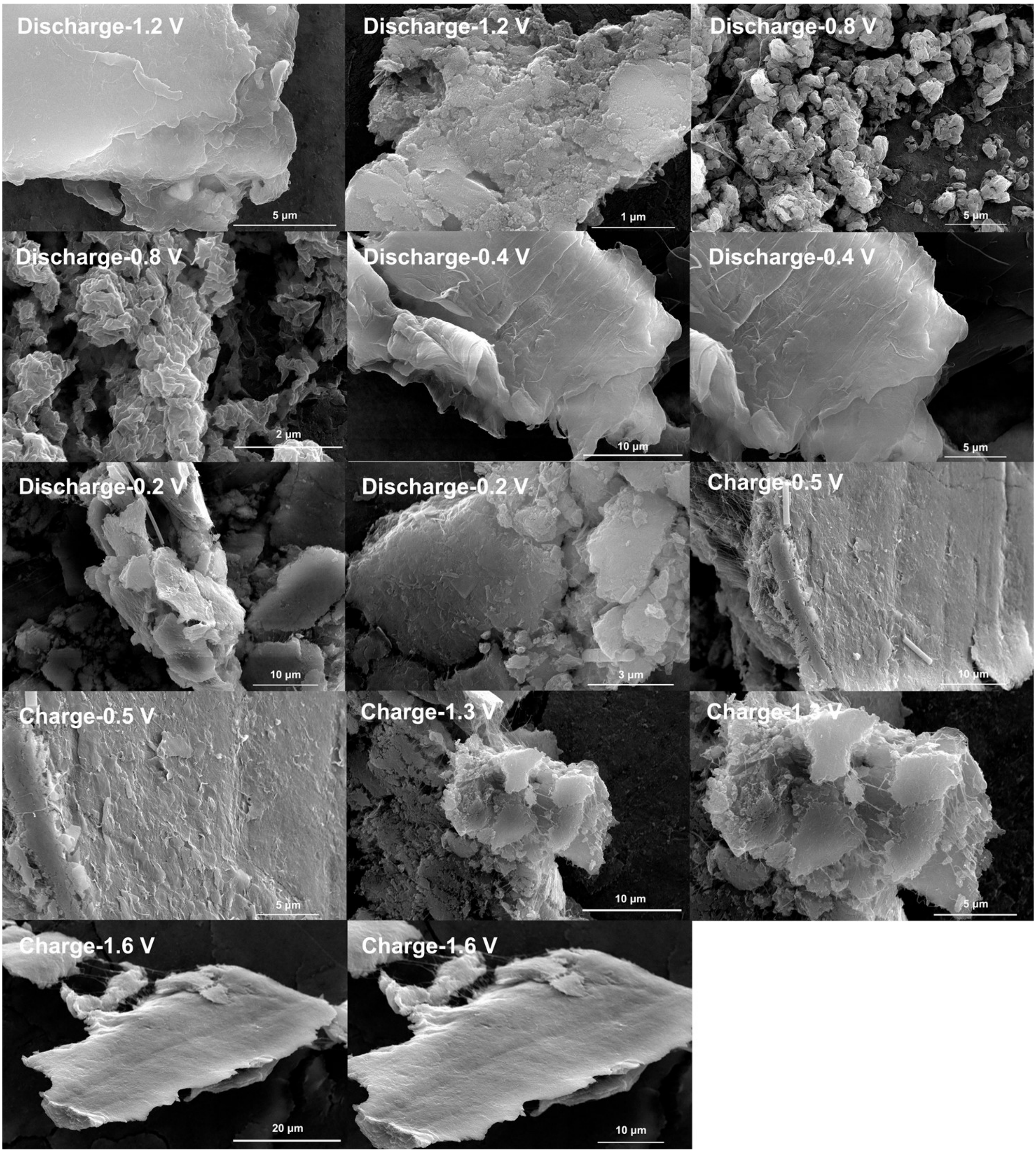

Fig. S15 ESEM images of the $Co_{0.14}V_2O_5 \cdot 0.95H_2O$ cathode at different discharge/charge states.

Table S1. The inductive coupled plasma emission spectrometry (ICP) results of $Co_xV_2O_5\cdot nH_2O$, $Ni_yV_2O_5\cdot nH_2O$, and $Cu_zV_2O_5\cdot nH_2O$.

Representation	Element	M (wt %)	Maximum Error (%)	Molar ratio and Chemical Formula
$Co_xV_2O_5\cdot nH_2O$	Co	3.9276	0.1884	$Co_{0.14}V_2O_5\cdot 0.95H_2O$
	V	47.3997	0.3857	
$Ni_yV_2O_5\cdot nH_2O$	Ni	3.9008	0.2589	$Ni_{0.15}V_2O_5\cdot 0.63H_2O$
	V	45.6545	0.7346	
$Cu_zV_2O_5\cdot nH_2O$	Cu	4.1276	0.4022	$Cu_{0.15}V_2O_5\cdot 0.60H_2O$
	V	45.0460	0.2504	

Three parallel tests were conducted, and the data presented in the table represent the averaged values of these tests. The maximum error was calculated based on the obtained results.

$$\text{Maximum Error (\%)} = \text{Max}\left[\frac{\left|\text{average value} - \text{ test value}\right|}{\text{average value}}\times 100\%\right]$$

where the average value was calculated based on the results from three independent tests.

Table S2. Comparison of electrochemical properties for vanadium-based cathodes.

Cathode Materials	Electrolyte	Specific capacity (mAh g^{-1})	Rate performance (mAh g^{-1})	Ref.
$Na_{0.33}V_2O_5$	3 M $Zn(CF_3SO_3)_2$	367 at 0.1 A g^{-1}	96.4 at 2 A g^{-1}	[16]
$K_2V_6O_{16}\cdot 2.7H_2O$	3 M $Zn(CF_3SO_3)_2$	361 at 0.1 A g^{-1}	178 at 20 A g^{-1}	[17]
$NaCa_{0.6}V_6O_{16}\cdot 3H_2O$	3 M $Zn(CF_3SO_3)_2$	347 at 0.1 A g^{-1}	154 at 5 A g^{-1}	[18]
$Ba_{1.2}V_6O_{16}\cdot 3H_2O$	2 M $ZnSO_4$	/	321.2 at 0.1 A g^{-1}	[19]
$Ca_{0.04}V_2O_5\cdot 1.74H_2O$	3 M $Zn(CF_3SO_3)_2$	/	311 at 0.5 A g^{-1}	[20]
$Na_{0.56}V_2O_5$	3 M $ZnSO_4$ and 0.5 M Na_2SO_4	317 at 0.1 A g^{-1}	91 at 2 A g^{-1}	[21]
$(NH_4)_2V_3O_8$/C	3 M $Zn(CF_3SO_3)_2$	356 at 0.1 A g^{-1}	232 at 0.5 A g^{-1}	[22]
$Ni_{0.22}V_2O_5$	3M ZnSO4	320 at 0.2 A g^{-1}	216 at 2 A g^{-1}	[23]
$Sr_{0.19}V_2O_5\cdot 1.3H_2O$/CNTs	3 M $Zn(CF_3SO_3)_2$	/	312 at 0.1 A g^{-1}	[24]
$VO_2\cdot 0.26H_2O$@rGO	3 M $Zn(CF_3SO_3)_2$	329 at 0.5 A g^{-1}	/	[25]
CaVO	2 M $ZnSO_4$	310 at 0.5 A g^{-1}	/	[26]
$Zn_{0.3}Na_{0.43}V_2O_5$	1 M $ZnSO_4$ and 1 M Na_2SO_4	326 at 0.2 A g^{-1}	209 at 1 A g^{-1}	[27]
$Na_6(V_{10}O_{28})\cdot 2.6H_2O$	2 M $Zn(CF_3SO_3)_2$	151.7 at 0.5 A g^{-1}	/	[28]
$(NH_4)0.77V_2O_5\cdot 0.8H_2O$	2 M $Zn(CF_3SO_3)_2$	/	366.2 at 0.05 A g^{-1}	[1]
$Co_{0.14}V_2O_5\cdot 0.95H_2O$	2 M $Zn(CF_3SO_3)_2$	373.2 at 0.05 A g^{-1}	338.2 at 0.1 A g^{-1}	**This work**

Supplementary Notes

Notes S1

The peak current (i) and the sweep rate (v) fit the below equation:[29]

$$i = av^{b}$$

and this equation can be rewritten as follows:

$$\log i = b\log(v) + \log(a)$$

where a and b are adjustable parameters, and the value of b is determined by the slope of the plot of log(*i*) versus log(*v*). In general, the kinetics of the electrode reactions in batteries can be evaluated based on the value of b. When the *b* value is close to 1, the electrode reaction is predominantly governed by capacitive behavior, whereas when the *b* value approaches 0.5, the kinetics of the electrode reaction are primarily controlled by diffusion processes.[30]

Notes S2

The ratio of the capacitive contribution could be described as the following equation:[31]

$$i = \mathrm{k}_1 v + \mathrm{k}_2 v^{1/2}$$

where $\mathrm{k}_1 v$ and $\mathrm{k}_2 v^{1/2}$ correspond to capacitive contribution and diffusion-controlled contribution, respectively.

Notes S3

Based on the GITT test data, the ionic diffusion coefficient (*D*) inside the battery can be calculated using the following equation:[32]

$$D_{Zn} = \frac{4}{\pi\tau}\left(\frac{m_B V_M}{M_B A}\right)^2 \left(\frac{\Delta E_s}{\Delta E_t}\right)^2$$

where τ and t represent the relaxation time (s) and the duration of current pulse (s), respectively. m_B is the mass of the active material. V_M is the molar volume (cm^3 mol^{-1}). M_B is the molar mass. A is the total contact area between the electrode and the electrolyte. ΔE_s and ΔE_t are the steady-state voltage change (V) by the current pulse and voltage change (V) during the constant current pulse (eliminating the voltage changes after relaxation time), respectively.

Notes S4

To gain deeper insight into the volumetric variation and reversibility of the electrode during the GCD process, the in situ optical microscopy (OM) characterization was conducted for the $Co_{0.14}V_2O_5 \cdot 0.95H_2O$ cathode during the first GCD cycle at a current density of 0.1 A g^{-1}. In the imaging of in situ OM (**Fig. 4**), Ti mesh as the current collector at the left imaging domain, with the $Co_{0.14}V_2O_5 \cdot 0.95H_2O$ cathode occupying the right portion of the Ti mesh. During the discharge process, as Zn^{2+} ions intercalate, a slight volumetric expansion of the electrode was observed along both lateral directions. The extent of the electrode's expansion increased progressively with the ongoing discharge process and the gradual uptake of Zn^{2+} ions, reaching its maximum volume when discharged to 0.2 V (**Fig. 4a-j**). Similarly, during the charging process, as Zn^{2+} ions de-intercalate, a subtle volumetric shrinkage was detected along both lateral directions. The degree of shrinkage became more pronounced as the charging process proceeded, culminating in the restoration of the electrode's pristine volume at 1.6 V, which matches its pre-discharge state (**Fig. 4k-p**). The unprocessed in situ OM video footage, along with its magnified playback segment, provide a more direct and vivid visualization of the volumetric changes and reversibility of the $Co_{0.14}V_2O_5 \cdot 0.95H_2O$ electrode throughout the above-mentioned GCD cycling process (**Video S1** and **S2**). The excellent structural stability of $Co_{0.14}V_2O_5 \cdot 0.95H_2O$ may stem from the robust layered architecture and minor structural strain, which endows it with a strong ability to accommodate volumetric changes during cycling. These findings further demonstrate that the synthesized $Co_{0.14}V_2O_5\cdot0.95H_2O$ cathode exhibits excellent structural stability and electrochemical performance.

References

1. Y. Liu, C. Lu, Y. Yang, W. Chen, F. Ye, H. Dong, Y. Wu, R. Ma and L. Hu, *Adv. Mater.*, 2024, **36**, 2312982.
2. G. Kresse and J. Furthmüller, *Computational Materials Science*, 1996, **6**, 15-50.
3. S. L. Dudarev, G. A. Botton, S. Y. Savrasov, C. J. Humphreys and A. P. Sutton, *Physical Review B*, 1998, **57**, 1505-1509.
4. P. E. Blöchl, *Physical Review B*, 1994, **50**, 17953-17979.
5. G. Kresse and D. Joubert, *Physical Review B*, 1999, **59**, 1758-1775.
6. J. P. Perdew, K. Burke and M. Ernzerhof, *Phys. Rev. Lett.*, 1996, **77**, 3865-3868.
7. J. P. Perdew and Y. Wang, *Physical Review B*, 1992, **46**, 12947-12954.
8. D. Kundu, B. D. Adams, V. Duffort, S. H. Vajargah and L. F. Nazar, *Nat. Energy*, 2016, **1**, 16119.
9. Q. Li, Y. Liu, K. Ma, G. Yang and C. Wang, *Small Methods*, 2019, **3**, 1900637.
10. Y. Kim, Y. Park, M. Kim, J. Lee, K. J. Kim and J. W. Choi, *Nat. Commun.*, 2022, **13**, 2371.
11. G. Yang, Q. Li, K. Ma, C. Hong and C. Wang, *J. Mater. Chem. A*, 2020, **8**, 8084-8095.
12. K. Zhu, T. Wu and K. Huang, *Chem. Mater.*, 2021, **33**, 4089-4098.
13. D. Dai, Y. Chen, B. Li, Z. Zhang, J. Wang, L. Wang, Y. Huang, B. Wang and D.-H. Liu, *Small*, 2025, **21**, 2408596.
14. H. Bandi, A. K. Kakarla, R. Dahule, R. Maezono, D. Narsimulu, R. Shanthappa and J. S. Yu, *Small*, 2025, **21**, 2408568.
15. Y. Lu, T. Zhu, W. van den Bergh, M. Stefik and K. Huang, *Angew. Chem. Int. Ed.*, 2020, **59**, 17004-17011.
16. P. He, G. Zhang, X. Liao, M. Yan, X. Xu, Q. An, J. Liu and L. Mai, *Adv. Energy Mater.*, 2018, **8**, 1702463.
17. B. Sambandam, V. Soundharrajan, S. Kim, M. H. Alfaruqi, J. Jo, S. Kim, V. Mathew, Y.-k. Sun and J. Kim, *J. Mater. Chem. A*, 2018, **6**, 15530-15539.
18. K. Zhu, T. Wu and K. Huang, *Adv. Energy Mater.*, 2019, **9**, 1901968.
19. X. Wang, B. Xi, X. Ma, Z. Feng, Y. Jia, J. Feng, Y. Qian and S. Xiong, *Nano Lett.*, 2020, **20**, 2899-2906.
20. M. Du, F. Zhang, X. Zhang, W. Dong, Y. Sang, J. Wang, H. Liu and S. Wang, *Science China Chemistry*, 2020, **63**, 1767-1776.
21. P. Gao, Q. Ru, H. Yan, S. Cheng, Y. Liu, X. Hou, L. Wei and F. Chi-Chung Ling, *ChemElectroChem*, 2020, **7**, 283-288.
22. H. Jiang, Y. Zhang, L. Xu, Z. Gao, J. Zheng, Q. Wang, C. Meng and J. Wang, *Chem. Eng. J.*, 2020, **382**, 122844.
23. M. Wei, W. Luo, D. Yu, X. Liang, W. Wei, M. Gao, S. Sun, Q. Zhu and G. Liu, *Ionics*, 2021, **27**, 4801-4809.
24. Y.-H. Du, X.-Y. Liu, X.-Y. Wang, J.-C. Sun, Q.-Q. Lu, J.-Z. Wang, A. Omar and D. Mikhailova, *Rare Metals*, 2022, **41**, 415-424.
25. L. Xie, W. Xiao, X. Shi, J. Hong, J. Cai, K. Zhang, L. Shao and Z. Sun, *Chem. Commun.*, 2022, **58**, 13807-13810.
26. J. Gao, C. Cheng, L. Ding, G. Liu, T. Yan and L. Zhang, *Chem. Eng. J.*, 2022, **450**, 138367.
27. M. Han, J. Zhi, J. Huang, W. Zhao, Y. Wu and P. Chen, *Cell Reports Physical Science*, 2023, **4**.
28. H. He, F.-C. Pan, X.-W. Liang, Q. Hu, S. Liu, J. Hu, S. C. Jun, D. Lin, Y. Yamauchi and Y. Huo, *Chem. Eng. J.*, 2023, **462**, 142221.
29. Y. Fu, Q. Wei, G. Zhang, X. Wang, J. Zhang, Y. Hu, D. Wang, L. Zuin, T. Zhou, Y. Wu and S. Sun, *Adv. Energy Mater.*, 2018, **8**, 1801445.
30. Y. Bai, C. Liu, T. Chen, W. Li, S. Zheng, Y. Pi, Y. Luo and H. Pang, *Angew. Chem. Int. Ed.*, 2021, **60**, 25318-25322.
31. B. He, Q. Zhang, P. Man, Z. Zhou, C. Li, Q. Li, L. Xie, X. Wang, H. Pang and Y. Yao, *Nano Energy*, 2019, **64**, 103935.
32. N. Zhang, F. Cheng, Y. Liu, Q. Zhao, K. Lei, C. Chen, X. Liu and J. Chen, *J. Am. Chem. Soc.*, 2016, **138**, 12894-12901.